Chapter 14
Thickness Estimation Using Multi-Frequency Acoustic Steady-State Excitation Spatial Spectroscopy

Joseph H. Lahmann, Erica M. Jacobson, Eric B. Flynn, and Adam J. Wachtor

Abstract Acoustic steady-state excitation spatial spectroscopy is a rapid, full-field nondestructive inspection technique that excites a structure with ultrasonic transducers and measures the complex out-of-plane surface response velocity over a prescribed inspection area using a scanning laser Doppler vibrometer. Through local wavenumber estimation of the resulting spatially resolved wavefield and correlation to Lamb wave dispersion curves, local material thickness can be estimated. Because dispersion characteristics vary with excitation frequency, wavenumber, and thickness, so too does the accuracy and spatial resolution of the thickness estimates. This work seeks to improve these metrics of thickness estimation by combining steady-state measurements collected at different excitation frequencies. Full-field inspection measurements for an aluminum plate were collected using excitation frequencies ranging from 50 kHz to 500 kHz in increments of 2 kHz. Using this set of measurements, several methods for error reduction by combining scans on a pixel-level were evaluated. The best performing method fused thickness estimations informed by the full correlation between the observed and expected wavenumber spectra, and resulted in consistent error reduction with an increasing number of scans and reduced the median error from 6.5% to 2.5%.

Keywords full-field acoustic nondestructive evaluation · structural health monitoring · laser Doppler vibrometer · guided waves · wavenumber estimation

Introduction

Ultrasonic inspection techniques have proven to be a valuable tool in a wide variety of nondestructive evaluation (NDE) applications, from in-situ quality assessment of additively manufactured parts [1, 2], to the inspection and quality control of lithium-ion batteries [3]. While versatile, many ultrasonic NDE methods either lack spatial resolution or require prohibitively long inspection times to function effectively as a structural health monitoring (SHM) tool [4]. Acoustic steady-state excitation spatial spectroscopy (ASSESS) has been shown to address both of these limitations, providing rapid and spatially resolved measurements suitable for both NDE and SHM applications [5–7]. In general, ASSESS excites a structure to a steady-state condition at a single frequency and scans the surface of the structure with a laser Doppler vibrometer (LDV) to measure the surface response velocity. From this measurement, it's possible to calculate the guided wavefield [8] and then estimate the amplitude of local wavenumbers present at each pixel across the inspection space. For plate-like structures, this local wavenumber estimation method and mapping has proven useful in the estimation of coating thickness [9], detection of composite delamination [5, 10], detection and localization of corrosion [11–13], and general thickness estimation [7, 14].

Joseph H. Lahmann
Department of Mechanical Engineering, University of Cincinnati, OH 45221
Engineering Institute, Los Alamos National Laboratory, NM 87545
e-mail: lahmanjh@mail.uc.edu

Eric B. Flynn
Space Remote Sensing and Data Science, Los Alamos National Laboratory, NM 87545
e-mail: eflynn@lanl.gov

Erica M. Jacobson · Adam J. Wachtor
Engineering Institute, Los Alamos National Laboratory, NM 87545
e-mail: ejacobson@lanl.gov; ajw@lanl.gov

Kristin B. Zimmerman, PhD (eds.), *Computer Vision and SLDV for Structural Dynamics, 2026, Vol. 6*, Conference Proceedings of the Society for Experimental Mechanics Series, https://doi.org/10.1007/978-8-743-81445-0_14

For a given excitation frequency, set of material properties, and plate thicknesses, Lamb-wave theory predicts the wavenumber and number of different modes present in the response signal [8]. Figure 1 shows an example of the expected dispersion behavior in terms of wavenumber and thickness for a 200 kHz excitation of an aluminum 6061 alloy. While Lamb-wave theory stems from infinite plates, guided wave modes will generally appear "Lamb-like" in a local region large enough to contain a few full wavelengths of the mode – which has been suggested to be around 3 wavelengths [13]. These dispersion characteristics can be leveraged to estimate local thickness of plate-like structures [14, 15]. Yet many challenges exist with thickness estimation through this framework, particularly in regard to dispersion characteristics. Firstly, there's a wavenumber dependency on the sensitivity of the thickness estimation. For localization, a higher wavenumber is usually preferable to allow a greater number of wavelengths for a given region in order to allow the developing modes to better approximate Lamb-wave behavior. Higher wavenumbers can be achieved through increasing excitation frequency, which subsequently shifts the scale of both axes in Figure 1: increasing the magnitude of the y-axis and scaling the x-axis so that new wave modes increasingly appear at thinner thicknesses. However, the appearance of higher wave modes can complicate the thickness estimation process as the same wavenumber values can be associated with different wave modes and thicknesses. While there have been several promising deep-learning based approaches to bypass some of these nuances [16, 17], there remain fruitful lines of exploration in the analytic domain.

Several approaches have been recently explored to address some of the issues associated with the existence of multiple wave modes present in the measurements and varying sensitivity of thickness estimation. The most common approach is to evaluate modes selectively, i.e. estimate through identifying and isolating the A0 mode or the S0 mode [14]. Moon et al. formalized the idea of wavenumber sensitivity and modal separation as candidates for selecting optimal excitation frequencies, informed through comparison of FEA simulations of guided wave patterns in flat plates [13]. To take advantage of the dispersion characteristics at different frequency-thickness products in characterizing structures with a broad range of thicknesses, information from different frequencies has been fused several ways. Kang et al. built on the approach of Moon et al., selecting 3 frequencies designed to ensure the presence of a wave mode with sensitivity above an acceptable threshold across a thickness range of interest. Each wave mode identified (A0 at 200 kHz, S0 at 450 kHz and S0 at 600 kHz) was filtered out and matched to the corresponding thickness. The final thickness estimate was taken as the average across all three scans [14]. Purcell et al. implemented a chirp signal between 75 kHz to 400 kHz to utilize broadband spectral information. The A0 mode was selected via a filter bank for each thickness corresponding to the expected wavenumbers across the spectrum of frequencies. The filter that maximized the signal energy of monogenic analysis in the time-domain corresponded to the estimated thickness. It was found that broad frequency information outperformed single-frequency, resulting in a mean percent error of 14.79 % for an 8 mm aluminum test plate with varying thicknesses [15]. While demonstrated to be effective in the cases reported, these methods purge the wavenumber information from modes outside of the isolated mode rather than leveraging the additional information and incorporating it into a single estimate.

These difficulties motivate the question which was addressed in this work: *How can information from separate scans across multiple frequencies be fused to improve general thickness estimates, while accounting for the full spectrum of guided wave modes?* The subsequent sections describe the collection of a dataset ranging in excitation frequency from 50 kHz to 500 kHz, detail the calculation of a thickness estimate from the collected wavefield data, and introduce several measurement

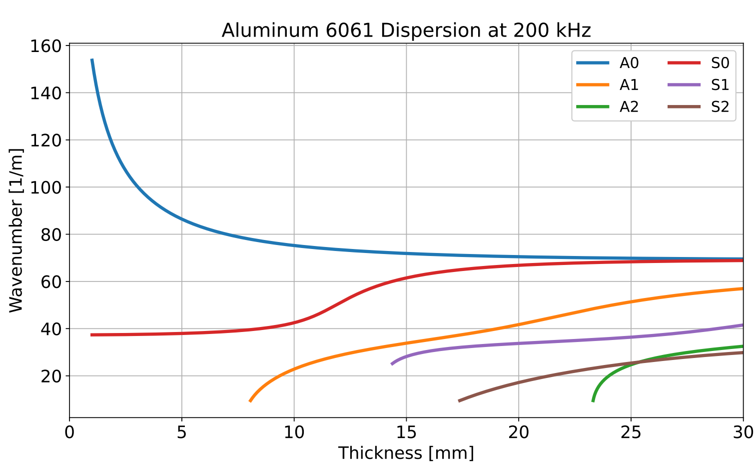

Fig. 1 Dispersion curve for aluminum 6061 at 200 kHz showing the relationship between wavenumber and structural thickness for multiple axisymmetric and symmetric modes.

fusion candidate methods for thickness estimation. These methods were compared over increasing numbers of randomly selected scan measurements to evaluate estimation error. The results indicated that fusing scans at the level of dispersion-curve similarity results in the highest potential for error reduction and defect localization.

Methods

The selected test specimen was a 10 mm aluminum 6061 plate containing a variety of manufactured thickness variations ranging from 1-10 mm in 1 mm increments, as shown in Figure 2. The diameter of the largest bores was 25 mm with varying thicknesses. The bottom row remained a constant 1 mm material thickness but decreased from 25 mm to 5 mm diameter in 5 mm increments. A transducer with rubber coupling was clamped at the bottom corner and driven with a narrow square-wave excitation at frequency, f_E, during collection. The plate was setup approximately 2 meters away from the measurement system and made level and perpendicular to the scanning head of the LDV in order to reduce distortion in the resulting wavefield. Co-registered LiDAR measurements captured the orientation of the plate normal and was used for a final data clean-up before performing wavenumber processing.

Examples of wavefield measurements from the scans that were collected from 50 kHz to 500 kHz in increments of 2 kHz are shown in Figure 3. A total of 225 independent scans were collected. One scan failed and the corrupted file was removed from the data set and also from subsequent analyses. Each scan took less than 25 seconds. With this data, a discrete vector of wavenumber and thicknesses of interest is defined, k_i and d_i respectively. Then local (pixel-wise) wavenumber was estimated by the application of a series of 2D log-Gabor filters centered at each value of k_i in the frequency-wavenumber domain,

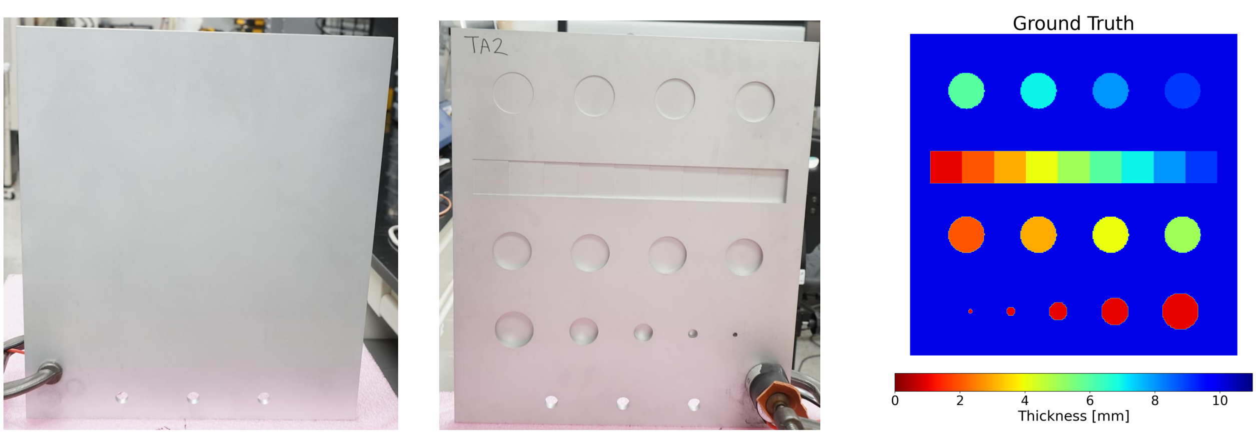

Fig. 2 Aluminum 6061 test plate containing a broad range of manufactured thickness defects. Left to right is the front (scanned side), back (thickness defects) and ground truth thickness map viewed from the front.

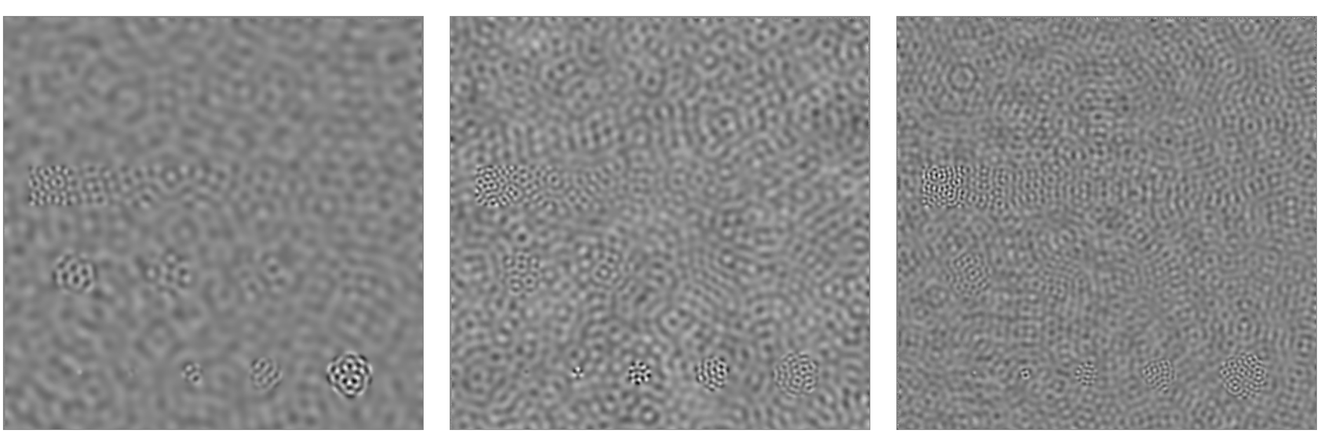

Fig. 3 Real components of complex ASSESS wavefield measurements collected at 200 kHz, 300 kHz, and 400 kHz (left to right).

inversion back to the time-space domain, and then calculation of the monogenic signal (essentially a filter-Hilbert method for complex signals) in the time domain [18]. The amplitude of the monogenic signal at each pixel for a given filter was estimated as the amplitude for that wavenumber, similar to [15]. To estimate local thickness, the resulting wavenumber spectrum was compared to the predicted thickness-wavenumber Lamb-wave dispersion curves for aluminum at each excitation frequency. This required a transformation of the wavenumber thickness dispersion curve into something more comparable.

For each mode present at thickness d, a Gaussian kernel Gabor filter was applied such that:

$$T[k,d] = \sum_m a_m[d] \cdot b_m[d] \cdot e^{\left(\frac{-(k_i - D_m[k,d])^2}{\beta(D_m[k,d]+0.001)^2}\right)} \tag{1}$$

Where T is the template, β is the filter bandwidth, $D_m[k,d]$ is the dispersion curve value for mode m at thickness d, and $b_m[d]$ is a scaling vector for higher order modes that ranges [0,1] over the first 2 mm that higher order modes are present. Furthermore, $a_m[d]$ is a second scaling factor that adjusts every mode relative to the amplitude of A0, given by:

$$a_m[d] = \frac{k_m[d]}{k_{A_0}[d]} \tag{2}$$

This results in scaling modes both according to entry and wavenumber value. Prior to use, the template was scaled to a Z-score resulting in a "simulated" spectrum seen in Figure 4.

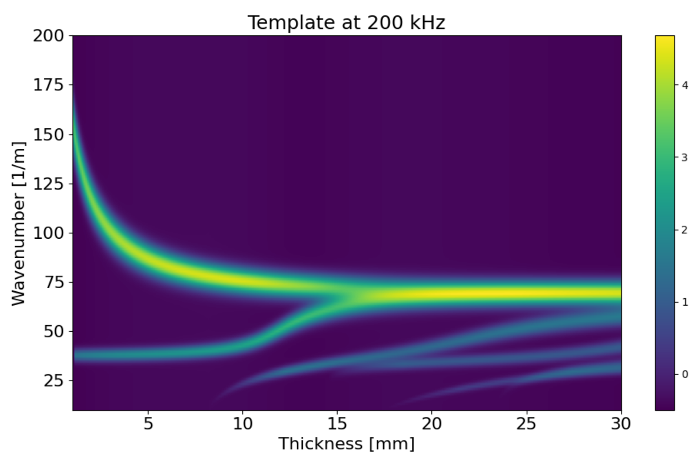

Fig. 4 A modified dispersion curve appropriate for comparison with the observed spectrum.

With this simulated spectrum, the Pearson's correlation coefficient can be calculated between the template and the estimated wavenumber spectrum, $\hat{K}$, across all interrogated thicknesses. This resulted in a correlation curve given by:

$$c[x,y,d] = \frac{T[k,x,y,d] \cdot \hat{K}[k,x,y]}{N} \tag{3}$$

where N is the number of thicknesses interrogated. To estimate the thickness, the thickness value corresponding to the maximum correlation at each pixel was calculated. The final estimate was cleaned by a median-filter of size 7x7 pixels.

Measurement Fusion Approaches

For a given set of scans, 4 primary methods of fusion were tested to improve thickness estimates. Two naïve approaches used were the statistical mean and median, defined in Eqn. 4 and Eqn. 5.

$$\hat{d}_{\text{mean}}[x,y] = \frac{1}{N}\sum_{i=0}^{N} \hat{d}_{f_i}[x,y] \tag{4}$$

$$\hat{d}_{\text{median}}[x,y] = \text{MED}\big(\hat{d}_{f_0}[x,y], \hat{d}_{f_1}[x,y], \ldots, \hat{d}_{f_N}[x,y]\big) \tag{5}$$

However, these approaches neglect to make use of the full correlation curve. This curve can be interpreted as a measure of how similar the observed wavenumber spectrum at a pixel is to the template representing the expected Lamb-wave spectrum, presenting information beyond the location of the maximum. One basic method of incorporating more of this information is to weight each thickness prediction with the raw amplitude of the maximum correlation, given by Eqn. 6.

$$\hat{d}_{\text{weighted mean}}[x, y] = \frac{\sum_{i=0}^{N} \max\big(c_{f_i}[x, y, d]\big) \cdot \hat{d}_{f_i}[x, y]}{\sum_{i=0}^{N} \max\big(c_{f_i}[x, y, d]\big)} \tag{6}$$

Here, c_{f_i} is the correlation between the observed wavenumber spectrum and template. A further extension would be to employ the full shape of the correlation curve, incorporating information about how similar the observed wavenumber spectrum is to every thickness. This method in general is described by Eqn. 7, which for a given set of scans will fuse each full correlation curve according to some function, prior to estimation via the maximum.

$$\hat{d}_{\text{fused correlation}}[x, y] = \arg\max_{d_i} \; f\big(c_{f_0}[x, y, d], c_{f_1}[x, y, d], \ldots, c_{f_N}[x, y, d]\big) \tag{7}$$

These methods were evaluated with sets of randomly selected frequencies. For 100 iterations, a random vector of excitation frequencies were selected and each fusion method was applied to the data with increasing numbers of scans, up to 6. Given that quality varied fairly widely in the experimental set, good performance from a fusion method should indicate robustness. For the full correlation curve fusion, only the results of a simple addition with raw correlation values are reported. While several other combinations of multiplying and scaling were explored, they resulted in nearly identical performance. Results were evaluated primarily according to absolute percent error (APE), given by:

$$\text{APE} = \left| \frac{d - \hat{d}}{d} \right| \times 100\% \tag{8}$$

which is calculated first for the entire plate. To gain a more targeted understanding of the performance, APE residuals were evaluated on the full plate, the 10 mm section of the plate (referred to as “plate”), and the defects. The defect areas were selected according to the ground truth map aligned by hand. Given the nature of the multi-scale defect plate and the sharp thickness changes from 10 to 1 mm at maximum, large absolute percent errors were expected in the residuals, resulting in a skewed distribution. Thus the summary statistics reported are the median APE (MAPE) and the 5th and 95th percentiles of the APE.

Results

The thickness calculations across all selected scans presented expected trends, *e.g.* increased spatial resolution was associated with higher values of the excitation frequency, Figure 5. At these higher frequencies, higher error was observed around the plate edge and boundaries of some of the defects. Because spatial sampling of points remains constant across all scans, this was to be expected. As shown in Figure 5, the residuals exhibited either general underestimation and overestimation.

Figure 6 shows the lowest error thickness estimate that the current single-frequency processing approach produced for the entire experimental dataset. Here the majority of thinner defects were clearly visible, but defect regions thicker than 6 mm quickly started to lose resolution, and the 9 mm thickness region and 5 mm diameter region were indistinguishable from the plate. Some neighboring frequencies resolved the smallest defect (as seen in Figure 5), but the shallow defect regions remained challenging to resolve at all frequencies.

Figure 7 compares the performance of each fusion method over successively larger sets of measurements collected at random frequencies. All the methods resulted in a decrease of the 95th percentile (worst-case performance), and a general improvement in median performance, but not necessarily the 5th percentile (best-case performance). When evaluating just the defect regions, each fusion method performed similarly, with the primary trend being a reduction in the spread of the error by increasing the number of scans. The full correlation method was the only method with a 5th percentile below a 5% residual for the defect regions and also exhibited monotonic reduction of error with increasing number of scans for all sections of the test plate. The largest improvement shown in Figure 7 was seen in the residuals of the plate. As such, the scan sets from the random selection experiment with the lowest MAPE for the plate were selected to examine in more detail.

The best thickness maps for plate estimation produced by the fusion methods are shown in Figure 8. Across all methods, the fused thickness estimates were much better at resolving the spatial features of the plate, especially for the shallower

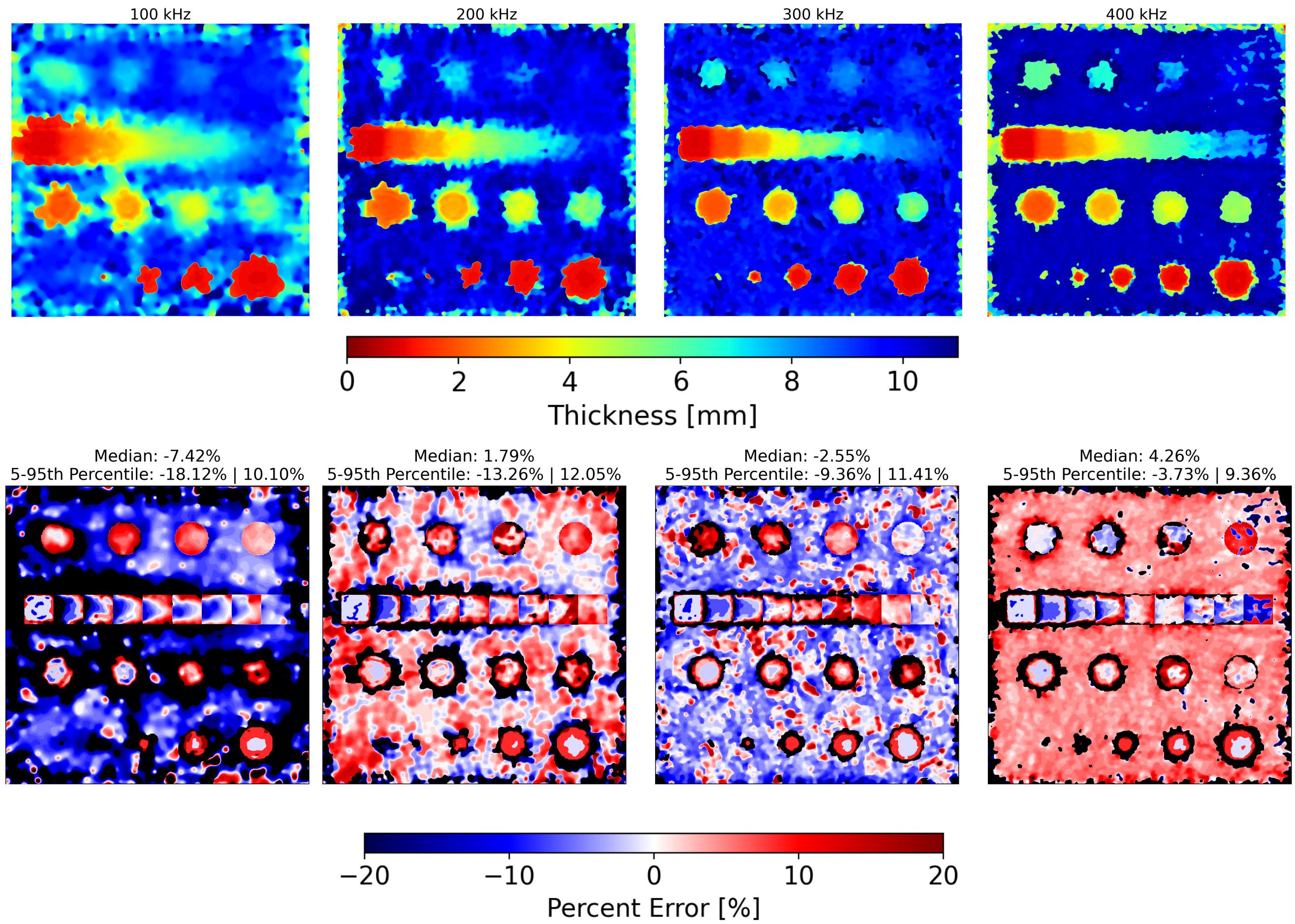

Fig. 5 Examples of single-frequency thickness estimates (top) and relative error (bottom) from 100, 200, 300, and 400 kHz excitation measurements

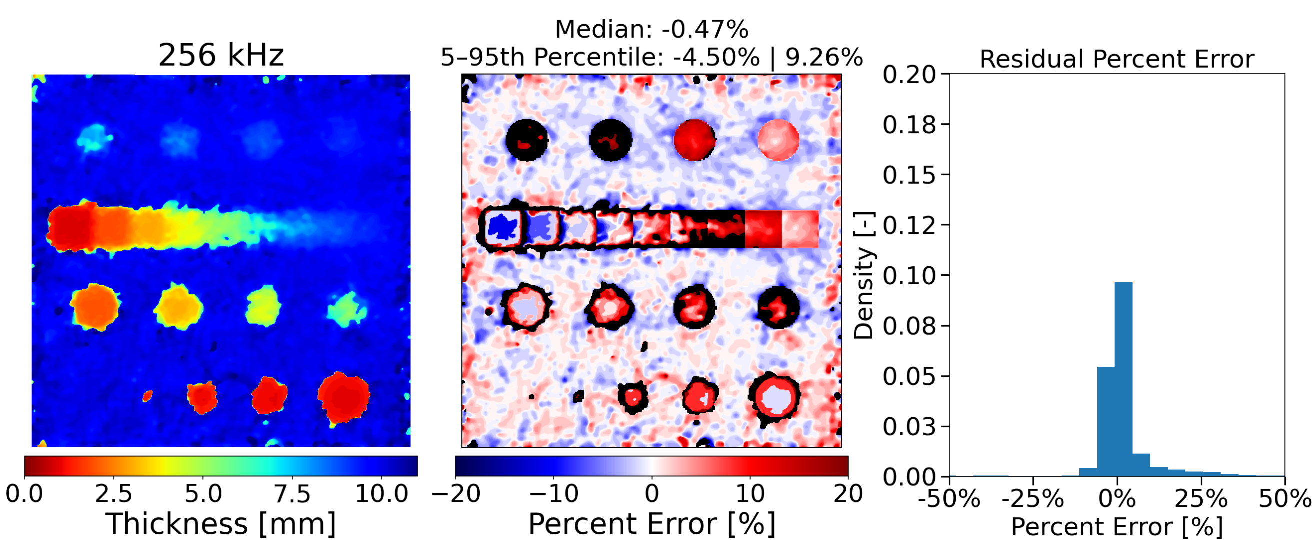

Fig. 6 The most accurate single frequency thickness estimate from the experimental set was collected at 256 kHz.

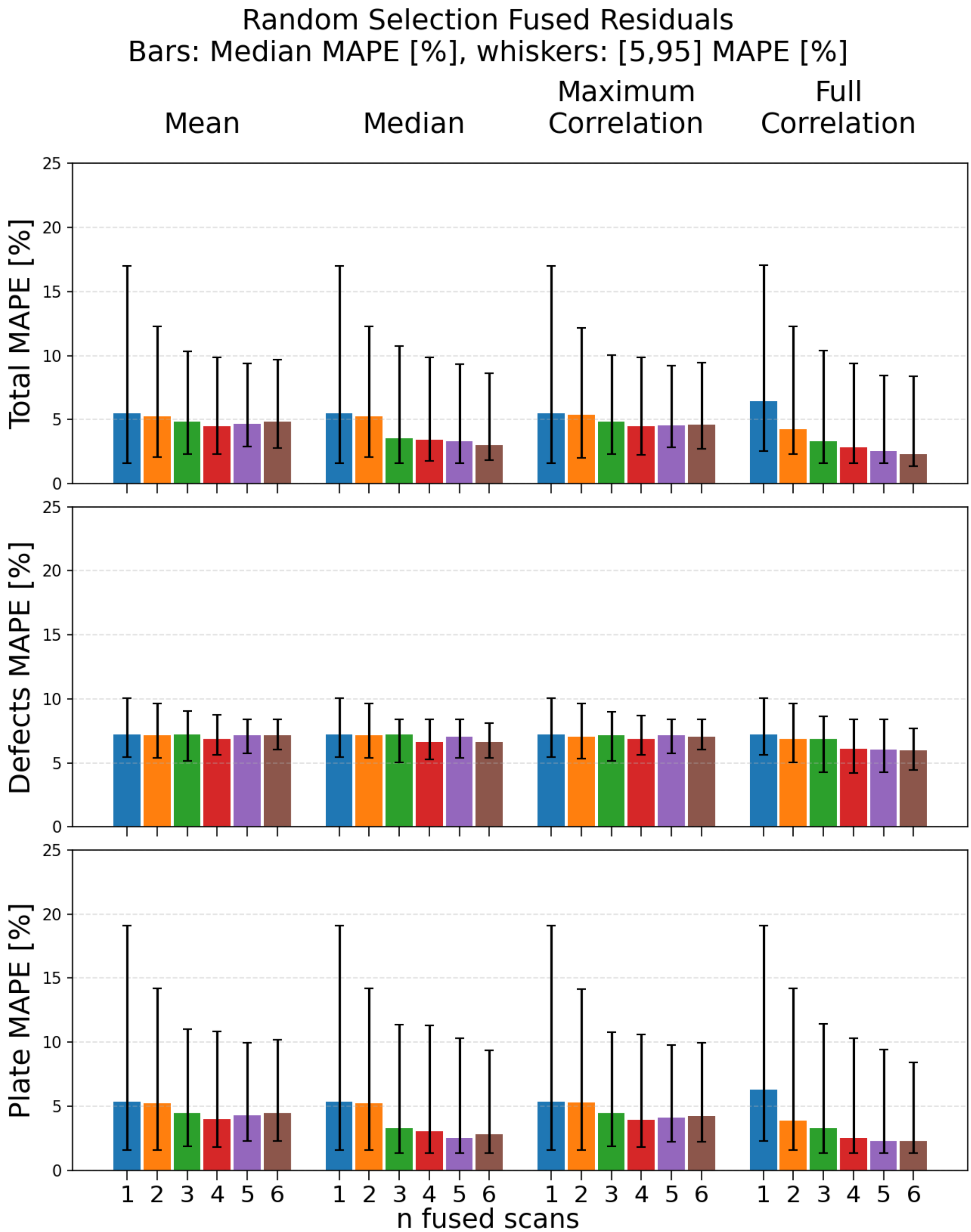

Fig. 7 The distribution of median residuals with increasing the number of scans fused. Each fusion condition is evaluated on the same 100 sets of randomly selected scans.

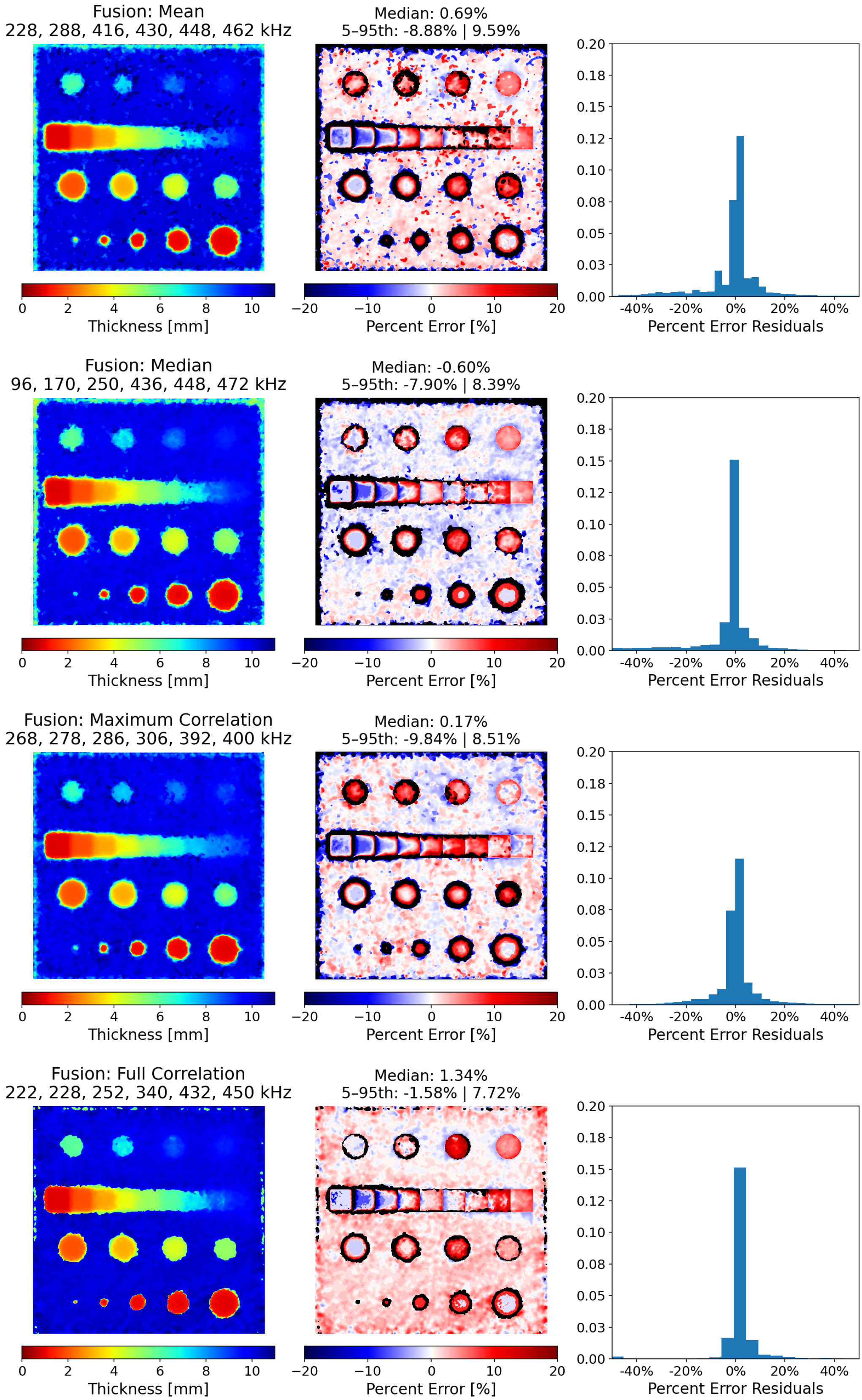

Fig. 8 The distribution of median residuals with increasing the number of scans fused. Each fusion condition is evaluated on the same 100 sets of randomly selected scans.

and narrower defects. As compared to the single scan baseline, percent error residuals had a much tighter distribution while the full correlation displayed the narrowest range, but resulted in slight overestimation. Another interesting point remains in the selection of scans for good performance. The median mechanism was the only method to use scans with values below 200kHz, which were found to be of generally lower quality and resolution. This was likely due to the mechanism of the median, which is effective at disregarding outliers.

Conclusion

This work investigated 4 methods of mearurement fusion for improving thickness estimation on an experimental dataset containing steady-state wavefield measurements that ranged from 50 kHz to 500 kHz in excitation frequency. Using the full correlation curve when combining estimates resulted in the best performance for resolving the nominal plate and full range of thickness reductions in the test sample. Because this method was tested on a dataset with varying scan quality, this performance indicated a higher robustness as compared to the other methods, which is attributed to its incorporation of more correlation information beyond just the maximum value. These results indicate a promising direction for maximizing the potential of analytic approaches to the estimation of thickness from guided-wave analysis.

References

1. Jacobson, E.M., Cummings, I.T., Fickenwirth, P.H., Flynn, E.B., and Wachtor, A.J. “Using steady-state ultrasonic direct-part measurements for defect detection in additively manufactured metal parts”. In Epp, D.S., editor, *Special Topics in Structural Dynamics & Experimental Techniques, Volume 5*, pages 59–73. Springer International Publishing (2022).
2. Cummings, I.T., Jacobson, E.M., Fickenwirth, P.H., Flynn, E.B., and Wachtor, A.J. “In-process defect detection for additively manufactured metal lattices”. In *Proceedings of the ASME 2020 International Mechanical Engineering Congress & Exposition*, volume 2A, pages 1–8 (2020).
3. Sun, B., Zhang, C., Liu, S., Xu, Z., and Li, L. “Ultrasonic inspection of pouch-type lithium-ion batteries: a review”. *Nondestructive Testing and Evaluation*, 39(6):1345–1378 (2024).
4. Yang, Z., Yang, H., Tian, T., Deng, D., Hu, M., Ma, J., Gao, D., Zhang, J., Ma, S., Yang, L., Xu, H., and Wu, Z. “A review on guided-ultrasonic-wave-based structural health monitoring: From fundamental theory to machine learning techniques”. *Ultrasonics*, 133:107014 (2023).
5. Flynn, E.B., Chong, S.Y., Jarmer, G.J., and Lee, J.R. “Structural imaging through local wavenumber estimation of guided waves”. *NDT & E International*, 59:1–10 (2013).
6. Cummings, I.T., Reinisch, E.C., Jacobson, E.M., Fraser, D.H., Wachtor, A.J., and Flynn, E.B. “Using lidar to identify planar measurement regions in ultrasonic inspections of complex structures”. In *Structural Health Monitoring 2021* (2022).
7. Shah, N., Jacobson, E.M., Flynn, E.B., and Wachtor, A.J. “Uncertainty quantification of thickness estimation via full-field ultrasonic inspection”. *Structural Health Monitoring 2023*, (0) (2023).
8. Rose, J.L. *Waves in Plates*, chapter 6, pages 76–106. Cambridge University Press (2014).
9. Ostiguy, P.C., Quaegebeur, N., and Masson, P. “Non-destructive evaluation of coating thickness using guided waves”. *NDT & E International*, 76:17–25 (2015).
10. Juarez, P.D. and Leckey, C.A.C. “Multi-frequency local wavenumber analysis and ply correlation of delamination damage”. *Ultrasonics*, 62:56–65 (2015).
11. Flynn, E.B. “Embedded multi-tone ultrasonic excitation and continuous-scanning laser Doppler vibrometry for rapid and remote imaging of structural defects”. In *7th European Workshop on Structural Health Monitoring* (2014).
12. Gao, T., Sun, H., Hong, Y., and Qing, X. “Hidden corrosion detection using laser ultrasonic guided waves with multi-frequency local wavenumber estimation”. *Ultrasonics*, 108:106182 (2020).
13. Moon, S., Kang, T., Han, S.W., Jeon, J.Y., and Park, G. “Optimization of excitation frequency and guided wave mode in acoustic wavenumber spectroscopy for shallow wall-thinning defect detection”. *J Mech Sci Technol*, 32(11):5213–5221 (2018).
14. Kang, T., Han, S.J., Moon, S., Han, S., Jeon, J.Y., and Park, G. “Lamb-wave sparse-frequency interdigital-transducer-based scanning laser Doppler vibrometry for quantitative depth-wise visualization of defects in plates”. *NDT & E International*, 107:102137 (2019).
15. Purcell, F.A.F., Eaton, M., Pearson, M., and Pullin, R. “Non-destructive evaluation of isotropic plate structures by means of mode filtering in the frequency-wavenumber domain”. *Mechanical Systems and Signal Processing*, 142:106801 (2020).
16. Eckels, J.D., Jacobson, E.M., Cummings, I.T., Fernandez, I.F., Ho, K., Dervilis, N., Flynn, E.B., and Wachtor, A.J. “Predicting local material thickness from steady-state ultrasonic wavefield measurements using a convolutional neural network”. *Ultrasonics*, 123:106661 (2022).
17. Yun, H., Feng, K., Rayhana, R., Pant, S., Genest, M., and Liu, Z. “A multidimensional data fusion neural network for damage localization using ultrasonic guided wave”. *IEEE Transactions on Instrumentation and Measurement*, 72:1–12 (2023).
18. Bridge, C.P. “Introduction to the monogenic signal”. *CoRR*, abs/1703.09199 (2017).